

Article

Effect of Rare Earth Cerium Content on Manganese Sulfide in U75V Heavy Rail Steel

Chao Zhuo, Rui Liu, Zirong Zhao, Yulei Zhang, Xiaoshuai Hao, Huajie Wu * and Yanhui Sun

Collaborative Innovation Center of Steel Technology, University of Science and Technology Beijing, Beijing 100083, China; beikezhuochao@163.com (C.Z.); a_liurui@163.com (R.L.); zirong1216@163.com (Z.Z.); zhangyulei02111996@163.com (Y.Z.); 18401619871@163.com (X.H.); sun_yanhui@163.com (Y.S.)

* Correspondence: wuhuajie@ustb.edu.cn; Tel.: +86-138-1080-6121

Abstract: To study the effect of Ce on the morphology of manganese sulfide, we added different contents of Ce into U75V heavy rail steel. The composition and morphology of sulfide in steel were analyzed. The inclusions' number, size, and aspect ratio were analyzed by automatic scanning electron microscope ASPEX. The results show that the inclusions in heavy rail steel without Ce are elongated MnS and irregular Al-Si-Ca-O inclusions. With the increase of Ce from 52 ppm to 340 ppm, the composition of main inclusions changes along the route of $\text{Ce}_2\text{O}_2\text{S-MnS} \rightarrow \text{Ce}_2\text{O}_2\text{S-MnS-Ce}_2\text{S}_3 \rightarrow \text{Ce}_2\text{O}_2\text{S-Ce}_3\text{S}_4\text{-Ce}_2\text{S}_3 \rightarrow \text{Ce}_2\text{O}_2\text{S-Ce}_3\text{S}_4\text{-CeS}$. Ce has a noticeable spheroidization effect on MnS, which can make inclusions finely dispersed. When Ce content is 139 ppm, the average size of inclusions is the smallest. The mechanism of Ce-modified MnS was discussed by combining experimental results with thermodynamic calculations. Finally, the effect of Ce treatment on inhibiting MnS deformation was verified by simulated rolling.

Keywords: U75V heavy rail steel; MnS; Cerium treatment; gleeble



Citation: Zhuo, C.; Liu, R.; Zhao, Z.; Zhang, Y.; Hao, X.; Wu, H.; Sun, Y. Effect of Rare Earth Cerium Content on Manganese Sulfide in U75V Heavy Rail Steel. *Metals* **2022**, *12*, 1012. <https://doi.org/10.3390/met12061012>

Academic Editor: Roumen Petrov

Received: 16 May 2022

Accepted: 11 June 2022

Published: 14 June 2022

Publisher's Note: MDPI stays neutral with regard to jurisdictional claims in published maps and institutional affiliations.



Copyright: © 2022 by the authors. Licensee MDPI, Basel, Switzerland. This article is an open access article distributed under the terms and conditions of the Creative Commons Attribution (CC BY) license (<https://creativecommons.org/licenses/by/4.0/>).

1. Introduction

U75V high-speed heavy rail steel is fine pearlite steel with high strength, toughness, and wear resistance. It exhibits high sensitivity to white spot, however, it is difficult to completely remove hydrogen from this type of steel. According to previous studies [1,2], an increase in the S content of steel or the presence of MnS can reduce the diffusion coefficient of hydrogen in steel, thereby mitigating the damage caused by hydrogen. However, due to the excellent deformation ability of MnS, the elongation of MnS along the rolling direction during the rolling process has become one of the essential factors causing excessive inclusions and inconsistencies in ultrasonic flaw detection. The large-size and long-striped structure of MnS induce anisotropy in steel and significantly reduce the transverse properties of the material. MnS inclusions initiate crack formation, which occurs at the interface between sulfide and the matrix under stress. With an increase in the load, the crack expands gradually along with the striped MnS inclusions [3,4]. Therefore, to improve the mechanical properties of heavy rail steel, it is particularly vital to control the morphology, size, number density, and distribution of MnS [5].

At present, there are generally two methods to control the morphology of MnS during the steelmaking process. The first method involves the formation of a mass of oxide inclusions in the molten steel by adding titanium, magnesium, zirconium, and other elements to promote the heterogeneous nucleation of MnS precipitates. This method allows the formations of small and dispersed MnS inclusions. Oikawa et al. [6] found that the size of MnS inclusions decreased significantly after adding Ti to Fe-0.1C-1Mn-0.02S steel. They proposed that the liquid nucleus of (Ti, Mn) O formed at the solid-liquid interface of steel serves as the heterogeneous nucleation site of MnS droplets. Xie et al. [7] reported that when the Mg content of 16MnCr5 steel was 35–42 ppm, numerous fine spindle-shaped or spherical composite inclusions with MgO-Al₂O₃ as the core and MnS as the shell were

formed in molten steel. The deformation degree of the inclusions after simulated rolling and forging was also small. Lu et al. [8] studied the distribution and morphology of MnS inclusions in Zr-containing non-quenched and tempered steel ingots and forging rods. Their results showed that when Zr content is 66 ppm, MnS is spherical or angular under two-dimensional and three-dimensional observation, and the distribution is uniform. The second method is the addition of calcium or rare-earth elements to S-containing steel to form smaller and lesser deformed sulfides in order to control the aspect ratio (the ratio of length to width of an inclusion) of inclusions. Another study [9] showed that the addition of a calcium alloy to steel can promote the transformation of sulfide from the striped to spindle structure, and that the ratio of calcium to sulfur content in steel ($w(\text{Ca})/w(\text{S})$) has a significant influence on the shape and length of the inclusions. When $w(\text{Ca})/w(\text{S}) > 0.2$, sulfide transforms to form a spindle structure, the average size of the inclusions decreases with the increase in $w(\text{Ca})/w(\text{S})$. Although MnS morphology control has been widely investigated [10–12], strategies to MnS formation are still limited. For example, Ti and Zr are not suitable for steel with a high oxygen content. Toward steel with low basicity refining slag, added Ca replaces Al_2O_3 in the refining slag and increases the Al content of steel to generate Al_2O_3 inclusions, which may lead to nozzle clogging [13]. The atomic size of rare earth elements is large and they easily lose their outer electrons, resulting in high activity. Thus, rare earth elements serve as good purifying agents and inclusion modifiers.

Cerium (Ce, a rare earth element), exhibits high activity and readily reacts with oxygen and sulfur in molten steel to form oxides and sulfides with a high melting point. Moreover, Ce can refine the grain size and improve the mechanical properties of the steel, and has a certain effect on harmful impurity elements such as phosphorus and arsenic [14–18]. Ren et al. [19] performed a thermodynamic calculation and found that the evolution order of inclusions was $\text{Al}_2\text{O}_3 \rightarrow \text{CeAlO}_3 \rightarrow \text{Ce}_2\text{O}_2\text{S} \rightarrow \text{Ce}_2\text{O}_2\text{S} + \text{CeS}$ when the Ce content of ultra-low carbon Al deoxidized steel increased from 0% to 0.028%, which was verified by laboratory experiments. Liu et al. [20] found that the primary inclusions changed from $\text{MgO} \cdot \text{Al}_2\text{O}_3$ -MnS to CeAlO_3 -MgO-MnS, $\text{Ce}_2\text{O}_2\text{S}$ -MgO-MnS, and $\text{Ce}_2\text{O}_2\text{S}$ -MnS after the addition of 0.014%, 0.024% and 0.037% Ce to EH36 steel, respectively. The addition of 0.024% Ce can inhibit the precipitation of pure MnS because Ce has a strong desulfurization ability. Liu et al. [21] found that 0.015% of added Ce could transform irregular MnS and Al_2O_3 inclusions in medium-carbon low-alloy steel to spherical $\text{Ce}_2\text{O}_2\text{S}$ and decrease the inclusion size. Liu et al. [22] applied spring steel as fasteners of high-speed rails; they found that the total oxygen content (T.O.) was at the lowest level when the Ce content was 0.045–0.065 wt%. Oversized and irregular sulfides and oxide inclusions transformed into rare earth oxides, sulfides, or oxygen sulfides that were spherical and had a size of $3 \mu\text{m}$. At present, the effect of Ce content on the inclusions in non-aluminum deoxidized U75V heavy rail steel has not been reported, and the mechanism underlying the modification effect of Ce on MnS in heavy rail steel remains to be studied.

2. Materials and Methods

The experiment was completed in a tubular Si-Mo resistance furnace. A 300 g U75V steel sample, taken from the casting billet and cut into small pieces, was put into a MgO crucible with an inner diameter of 40 mm and an outer diameter of 48 mm. A graphite crucible was coated on the MgO crucible to protect the furnace. The schematic diagram of the resistance furnace and the composition of molten steel are shown in Figure 1 and Table 1.

Table 1. Chemical composition of U75V steel (%).

Composition	C	Si	Mn	P	S	V	Als
Content	0.77	0.64	0.89	0.02	0.007	0.04	0.0015

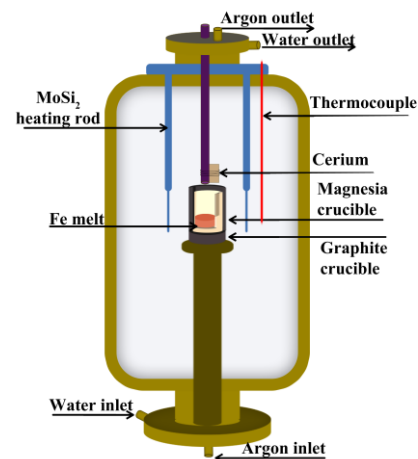


Figure 1. Schematic diagram of silicon molybdenum tube furnace.

The schematic diagram of the experimental process is shown in Figure 2a. After the crucible was placed, the upper lower ends of the furnace were closed; the temperature of the resistance furnace was set as shown in Figure 2a. When the temperature reached 1600 °C, it was held for 30 min to ensure that the steel blocks were melted and completely homogenized. Then, Ce was wrapped with pure iron foil and added to the molten steel without stirring. Five levels of Ce content, 52 ppm, 139 ppm, 171 ppm, 256 ppm, and 340 ppm, were used to study the effect of Ce content on inclusions in heavy rail steel. After holding for 15 min, the temperature began to decrease. When the temperature dropped to 700 °C, the power was cut off, and then the resistance furnace was cooled to room temperature by furnace cooling. In total, 2.5 L/min argon was injected throughout the experiment.

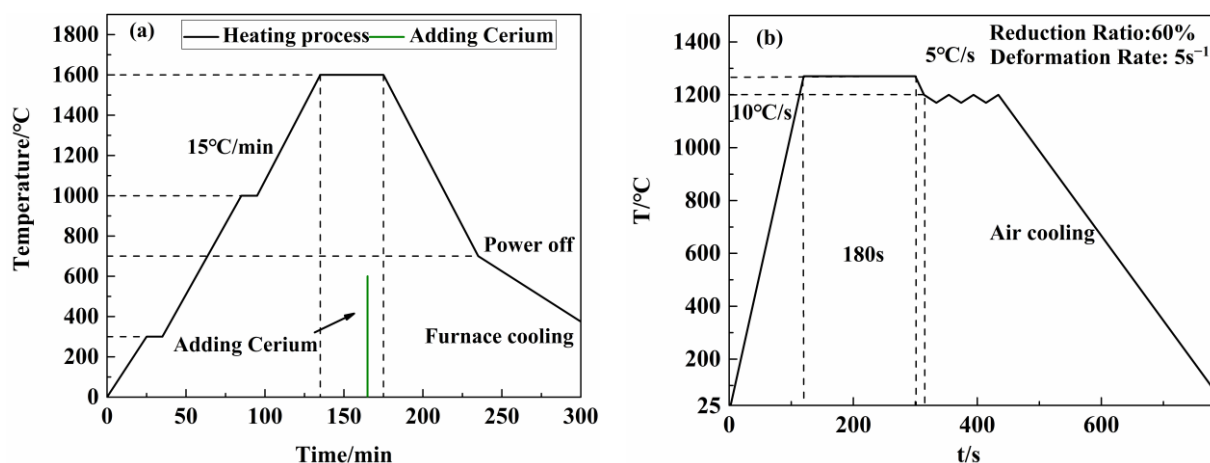


Figure 2. Temperature setting, (a): resistance furnace; (b): gleeble–3500 simulated rolling mill.

The ingot was cut into a cylindrical sample of $\varnothing 8 \times 15$ mm, which was used for the rolling simulated experiment. The temperature system refers to the production process of a plant, as shown in Figure 2b. The deformed samples were cut, polished, and observed with ASPEX. The simulation rolling experiment was completed on gleeble-3500 thermal simulation testing machine (Dynamic Systems Inc., Poestenkill, NY, USA).

The Ce content was measured by the ICP method. The composition, quantity, size, and aspect ratio of inclusions were analyzed by an ASPEX automatic scanning electron microscope (FEI, Hillsboro, OR, USA) after the ingot was ground and polished. The sampling position, analysis surface, and random observation position are shown in Figure 3, which reduces the influence of S element segregation inside the ingot. The scanning area of each sample was about 10 mm², and the minimum size of inclusions scanned

was 1 μm . The inclusion morphology was observed by a ZEISS electron microscope equipped with an EDS (Energy Dispersive Spectrometer) model of Gemini SEM 500 (Zeiss, Niedersachsen, Germany). The extraction of inclusions was conducted by electrolysis with anhydrous organic solution, and the electrolyte was 10% AA solution (a mixed solution of 1% tetramethylammonium chloride-10% acetylacetone-89% methanol). Figure 4 is the schematic diagram of the electrolytic cell. The current density was 0.04 A/cm^2 and the temperature was $0\sim 5 \text{ }^\circ\text{C}$. The electrolysis time was 4 h. After electrolysis, the filtered membrane was filtered with Polytetrafluoroethylene (PTFE) filter membrane. After spraying gold on the filtered membrane, the three-dimensional characteristics of inclusions were observed by field emission scanning electron microscopy. Table 2 shows the Ce content in each sample, where C0 is the control group without Ce addition.

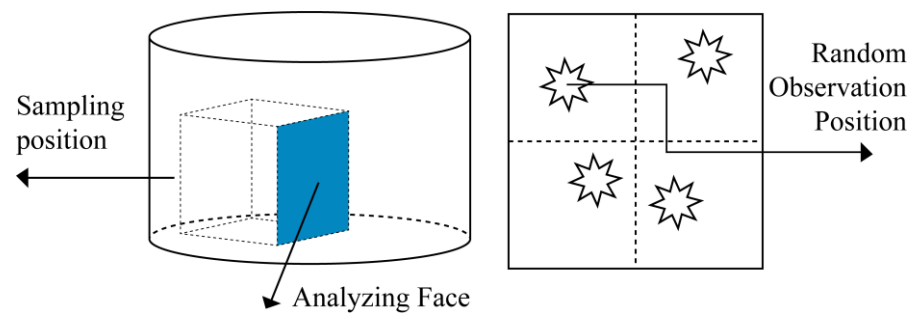


Figure 3. Sampling place, analyzing face, and random observation position.

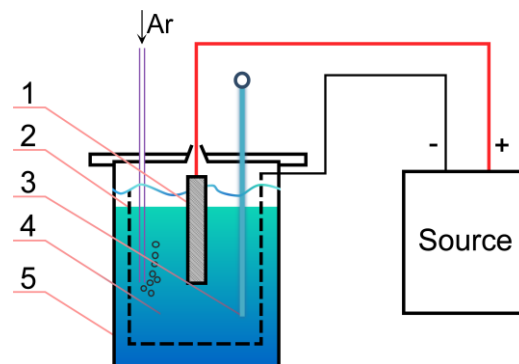


Figure 4. Schematic diagram of inclusion extraction (1—anode; 2—cathode; 3—thermometer; 4—electrolytes; 5—beaker).

Table 2. Ce content of each sample (mass%).

No.	C0	C1	C2	C3	C4	C5
Ce	0	0.0052	0.0139	0.0171	0.0256	0.0340

3. Results and Discussion

3.1. Composition and Morphology of Inclusions

Figure 5 shows the morphology and elemental mapping profiles of typical inclusions with different Ce contents. Figure 5a,b shows the control group C0 without Ce treatment. The inclusions are mainly large-scale irregular striped MnS and spherical $\text{Al}_2\text{O}_3\text{-SiO}_2\text{-CaO}$ inclusions. After Ce treatment, the inclusions in steel convert to oxygen sulfides or Ce sulfides, which is in agreement with the result reported by Adabavazeh et al. [15] and Gao et al. [23]. Because of the low wettability and large contact angle between Ce-containing inclusions and molten steel [15], the inclusions in molten steel are ellipsoidal, and their size is markedly reduced. When the Ce content was 52 ppm, the primary inclusion type was $\text{Ce}_2\text{O}_2\text{S}$ that formed the core, with a small amount of MnS composite inclusions precipitated

on the surface, as shown in Figure 5c. In addition to the $\text{Ce}_2\text{O}_2\text{S}$ -MnS composite inclusions, Ce_xS inclusions were observed when Ce content was 139 ppm and 171 ppm, as shown in Figure 5d. However, when the Ce content was approximately 256 and 340 ppm, the typical inclusions were single $\text{Ce}_2\text{O}_2\text{S}$ inclusions and composite $\text{Ce}_2\text{O}_2\text{S}$ and Ce_xS inclusions, as shown in Figure 5e,f. MnS was rarely precipitated on the surface of $\text{Ce}_2\text{O}_2\text{S}$, because with the increase in the Ce content, a large amount of S is consumed by the $\text{Ce}_2\text{O}_2\text{S}$ and Ce_xS inclusions, causing the actual concentration of $[\text{S}][\text{Mn}]$ in molten steel to not reach the equilibrium concentration.

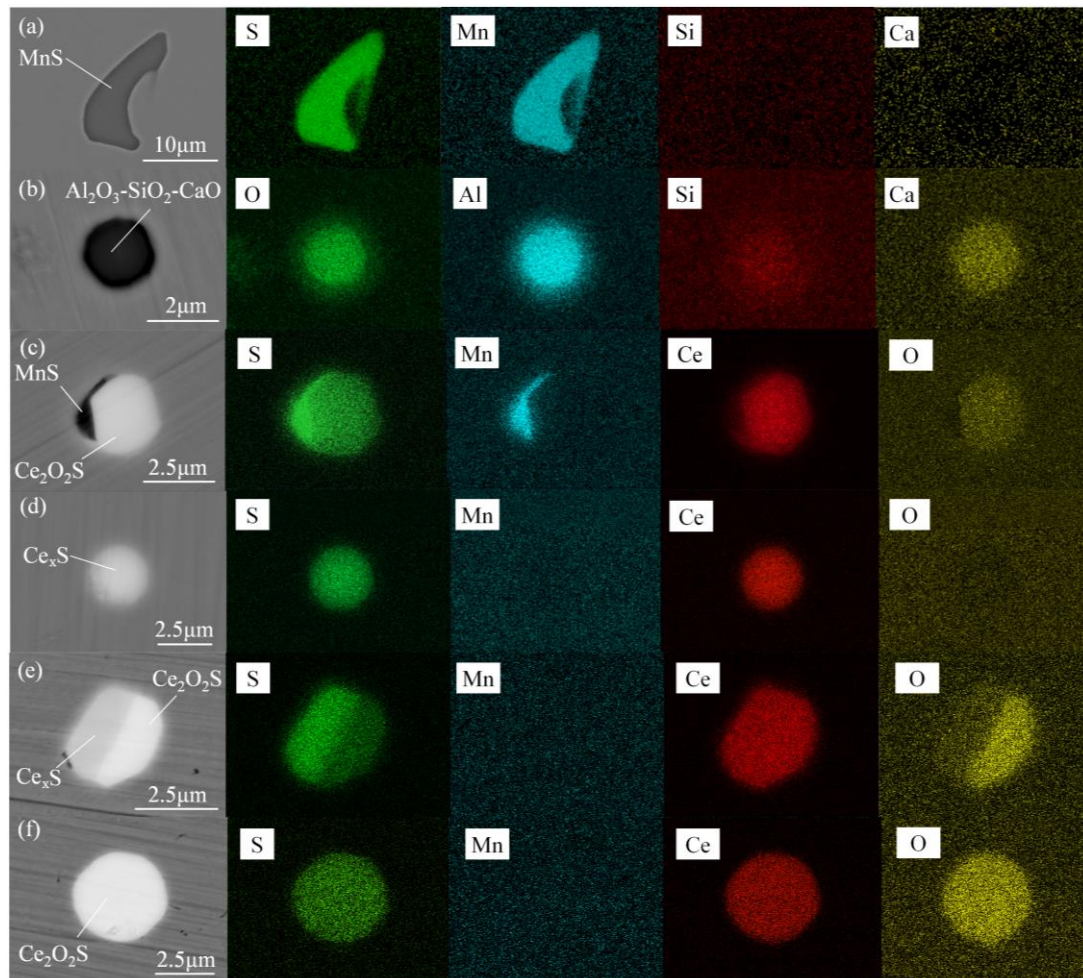


Figure 5. Morphology and elemental mapping of typical composite inclusions: (a,b) 0 ppm, (c) 52 ppm, (d) 139 ppm, 171 ppm, (e,f) 256 ppm, 340 ppm.

The three-dimensional morphology of typical inclusions with different Ce contents is shown in Figure 6. Figure 6a shows the morphology of MnS in the steel without Ce addition; it can be seen that MnS is irregular and large. When the Ce was 52 ppm, the typical inclusion was an ellipsoidal composite, with $\text{Ce}_2\text{O}_2\text{S}$ as the core, and a small amount of MnS precipitates on the surface. No single irregular MnS precipitates were observed, as shown in Figure 6b. Figure 6c,d shows that the $\text{Ce}_2\text{O}_2\text{S}$ -MnS- Ce_xS composite inclusions and the $\text{Ce}_2\text{O}_2\text{S}$ -MnS inclusions appear when the Ce content of molten steel was 139 and 171 ppm, in addition to near-spherical Ce_xS inclusions. When the Ce content was 256, and 340 ppm, the inclusions in the steel were mainly single $\text{Ce}_2\text{O}_2\text{S}$ and $\text{Ce}_2\text{O}_2\text{S}$ - Ce_xS , as shown in Figure 6e,f. It is worth mentioning that in Figure 6c, the inclusion comprised $\text{Ce}_2\text{O}_2\text{S}$ as the core, with the surface precipitation of MnS and Ce_xS composite inclusions. These type of inclusions are not observed in the two-dimensional morphology, indicating that

three-dimensional morphology can more accurately reveal the type of inclusions. It can be found that the variation trend of inclusions is similar to that illustrated in Figure 5.

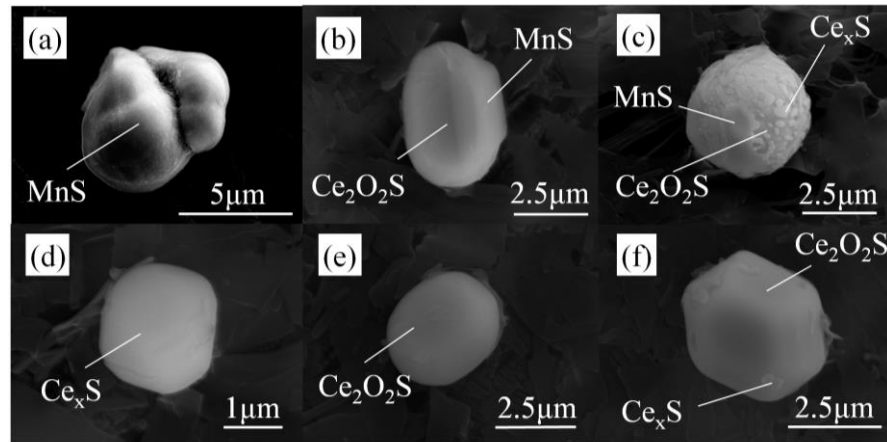


Figure 6. Three-dimensional morphology of typical inclusions in steel samples: (a) 0 ppm, (b) 52 ppm, (c,d) 139 ppm, 171 ppm, 256 ppm, (e,f) 340 ppm.

The typical inclusion types of each sample obtained after electron microscopy were classified and counted; the results are summarized in Table 3. When the Ce content was 52 ppm, the striped MnS disappeared. Nonetheless, the Ce content must be optimized on the basis of the size, number density, and aspect ratio of inclusions.

Table 3. Types of inclusions in different heats.

Typical Inclusions	Si-Al-Ca-O	MnS	Ce ₂ O ₂ S-MnS	Ce _x S	Ce ₂ O ₂ S	Ce ₂ O ₂ S-Ce _x S	Ce ₂ O ₂ S-Ce _x S-MnS
C0	√√	√√	–	–	–	–	–
C1	–	–	√√	–	–	–	–
C2	–	–	√√	√	–	–	√
C3	–	–	√√	√	√	√	√
C4	–	–	√	√	√	√√	–
C5	–	–	√	√	√	√√	–

√√: the main type of inclusions, √: a small number of inclusions.

3.2. Number Density, Size, and Aspect Ratio of Inclusions

To quantitatively characterize the inclusions in the steel sample, the number density, average size, and aspect ratio of the inclusions were calculated, the results are shown in Figures 7 and 8.

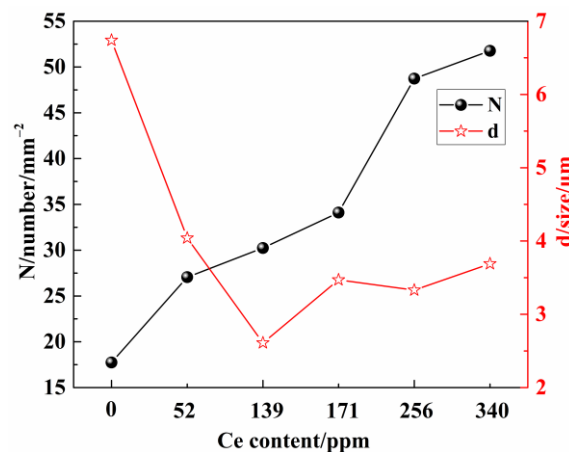


Figure 7. Number density and the average size of inclusion.

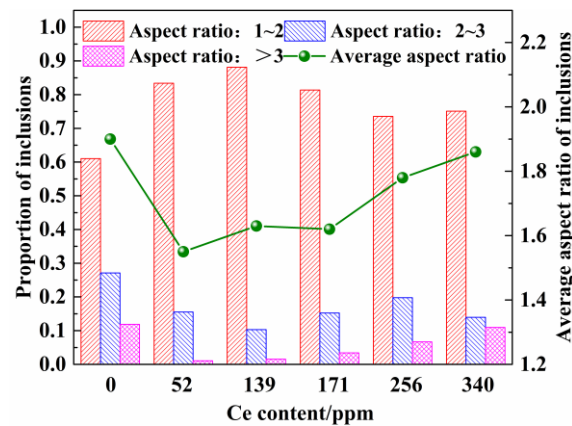


Figure 8. Aspect ratio of inclusions.

Figure 7 shows the changes in the number density and size of inclusions in different samples. Ce addition was found to significantly increase the number density of the inclusions in molten steel. When Ce was not added, the number density of the inclusions was $17.74/\text{mm}^2$. With an increase in the Ce content, the number density of the inclusions increased, reaching a maximum of $51.76/\text{mm}^2$ at 340 ppm Ce. In addition, Ce addition can significantly reduce the size of the inclusions. The average size of the inclusions before Ce addition was $6.74\ \mu\text{m}$, whereas after Ce addition it was $3.22\text{--}4.16\ \mu\text{m}$. Unlike the number density, the average size of the inclusions first decreased and then increased with an increase in the Ce content, which agrees with the result of Luo [24] and Wang [25]. Because of the change of free energy, the free energy of O and S binding in Ce and steel is considerably lower than that of S and Mn binding; thus, rare earth oxygen sulfides are easily generated [26]. Moreover, the melting point of rare earth sulfides is higher than that of MnS, and they precipitate before MnS during the solidification process. The continuous consumption of S reduces the activity of S in steel, which significantly affects the combination of Mn and S, thereby decreasing the core of heterogeneous nucleation, and reducing the probability of the transformation of single-particle MnS inclusions to large MnS inclusions under high supersaturation conditions. When the Ce content was high or excessive, the addition of excessive Ce enhances the binding ability of rare earth elements to the formation elements of the inclusions, resulting in the formation of a large number of rare earth inclusions. The inclusion collision and aggregation probabilities increase sharply; therefore, the inclusion size increases gradually.

The effect of the Ce content on the aspect ratio of the inclusions is shown in Figure 8. The average aspect ratio of the inclusions decreased significantly after Ce addition. The aspect ratio of the inclusions without Ce was 1.9, whereas for the inclusions with Ce it was between 1.55 and 1.86. The average aspect ratio of the inclusions increases with the Ce content. The proportion of the inclusions with an aspect ratio between one and two increased significantly after Ce treatment. The proportion of inclusions with an aspect ratio between two and three and >three decreased, indicating that Ce addition induces an apparent spheroidization effect on the inclusions. However, when the Ce content is excessive, i.e., more than 256 ppm, the proportion of the inclusions with an aspect ratio between one and two decreased gradually, whereas the proportion of the inclusions with an aspect ratio between two and three increases gradually. This trend is observed because inclusion collision and aggregation lead to an irregular shape and size enlargement. It indicates that excessive Ce content is not conducive to the dispersion and fine control of the inclusions. According to the number density, size, and aspect ratio of the inclusions, many fine and dispersed ellipsoidal inclusions can be generated at 139 ppm Ce.

3.3. Thermodynamic Analysis of Inclusion Formation in Steel

The precipitation of each sample during the cooling process was calculated by FactSage8.1, a thermodynamic calculation software; the result is shown in Figure 9. The inclusions without Ce were primarily the Al_2O_3 - SiO_2 - MgO and MnS . When the Ce content was 52 ppm, a large amount of dispersed $\text{Ce}_2\text{O}_2\text{S}$ was formed at 1600 °C. $\text{Ce}_2\text{O}_2\text{S}$ acts as a heterogeneous nucleation core during the cooling process of molten steel, which facilitates MnS precipitation on its surface and avoids the formation of long-striped MnS . As can be seen in Figure 9c, when the Ce content was 139 ppm, CeS began to form at high temperatures. During the cooling process, CeS was first converted to Ce_3S_4 and finally to Ce_2S_3 near the liquidus temperature. With a further increase in the Ce content by 171 ppm, the $\text{Ce}_2\text{O}_2\text{S}$ content slightly changed, the Ce_2S_3 content increased gradually, and the amount of MnS precipitates decreased gradually, as shown in Figure 9d. As shown in Figure 9e,f, when the Ce content was 256 and 340 ppm, MnS precipitation did not occur at all, and the stable sulfide phase of solidified Ce was changed from single Ce_2S_3 to Ce_2S_3 , Ce_3S_4 , and CeS and Ce_3S_4 , respectively, which is consistent with the analysis results of the abovementioned inclusion morphology. Through the above analysis, we confirm that Ce plays a role in mitigating the formation of long-striped MnS through two ways: (1) Ce induces the precipitation of MnS on the surface of sulfur oxides, and (2) the total amount of MnS precipitates is reduced upon S consumption.

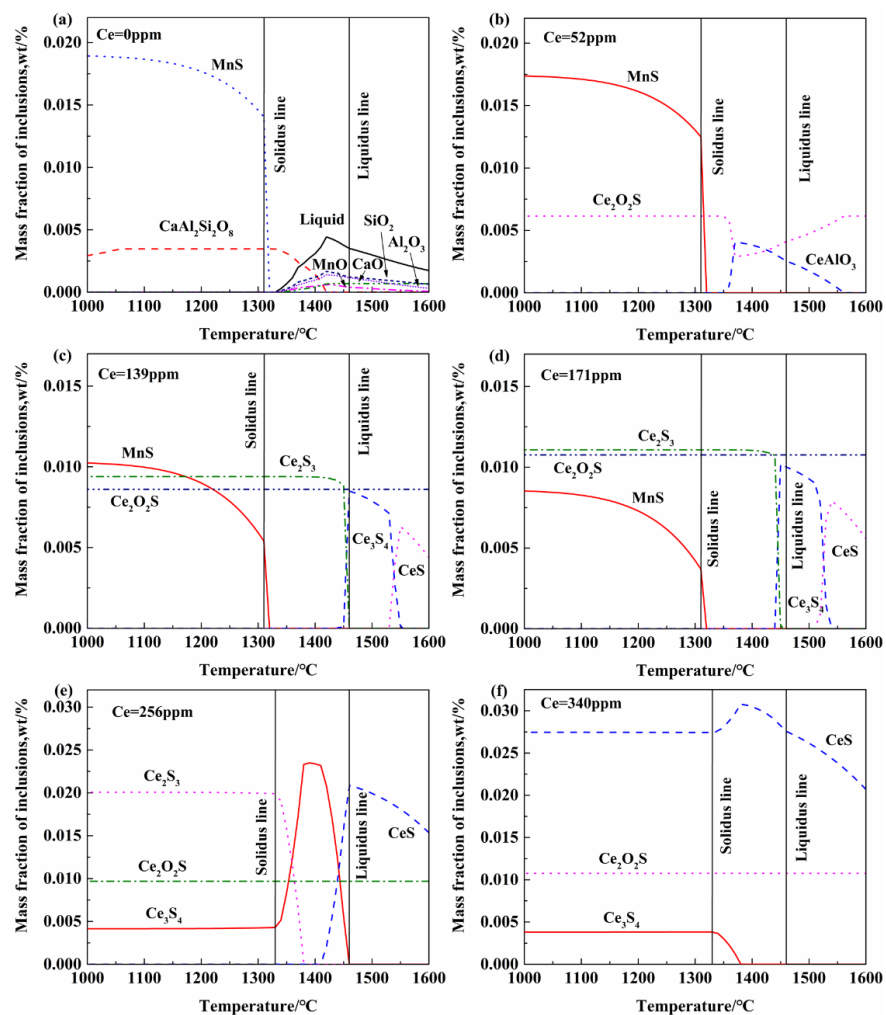


Figure 9. Evolution of inclusions during solidification with different Ce contents: (a) 0 ppm, (b) 52 ppm, (c) 139 ppm, (d) 171 ppm, (e) 256 ppm, (f) 340 ppm.

3.4. Evolution Mechanism of Inclusions in Heavy Rail Steel after Adding Ce

Based on the thermodynamic calculation and the experimental results, the evolution mechanism of the inclusions in U75V heavy rail steel after Ce addition was investigated, as illustrated in Figure 10. According to the composition and morphology analysis of the inclusions, mass $\text{Ce}_2\text{O}_2\text{S}$ phases exist in the inclusions upon Ce addition, which mainly have two sources. (1) The entry of Ce into molten steel and its combination with O and S in the molten steel, which can be expressed as Equation (1) [27], and (2) the modification of the $\text{SiO}_2\text{-Al}_2\text{O}_3\text{-CaO}$ inclusion upon Ce addition. When Ce is not added to molten steel, the inclusions at high temperature mainly comprise the $\text{SiO}_2\text{-Al}_2\text{O}_3\text{-CaO}$ system. These inclusions are generally large and irregular in shape, while MnS is precipitated during solidification [28]. Therefore, Ce added to the molten steel first diffuses to the interface between the oxide inclusions and molten steel in the form of atoms, followed by their conversion to the ionic form and attachment to the surface of the oxide inclusions. Second, Ce ions react with the active sites on the oxide surface, and reaction products CeAlO_3 and Ce_2O_3 adhere to the surface of the original inclusion in the form of a liquid film and grow. As the reaction proceeds, Ce and O in the molten steel continue to diffuse into the interface; the reaction proceeds smoothly, with an increase in the thickness of the liquid film. Once the liquid film reaches a specific thickness, it solidifies and aggregates into spheres according to the principle of minimum surface energy [26]. Thus, a composite inclusion with Si-Al-Ca-O as the core and Ce-Si-Al-Ca oxide as the surface is formed. Al and Si in the inner layer also diffuses to the outer layer with further reaction. Ce ions continue to diffuse to the inner layer, and the required diffusion driving force increases accordingly. At this stage, the ion exchange process of Ce and Al, Si and Ca slows down. Till the end of the diffusion process of internal and external ions, Ce completes the modification of Al-Si-Ca oxide in steel, which can be expressed as Equation (2) [29]. At this stage, the content of Ce in molten steel is sufficient to allow the reaction between Ce oxide S in molten steel, generating oxygen sulfide, which can be expressed as Equation (3) [30].

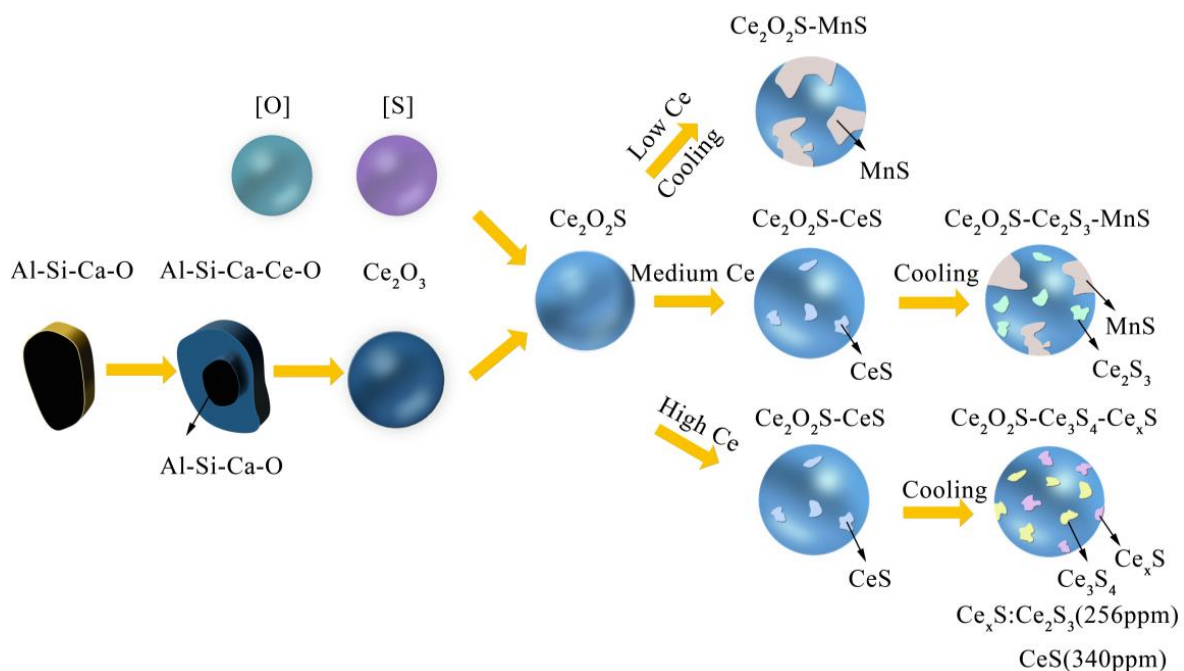
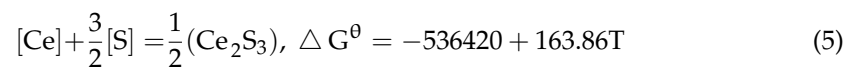
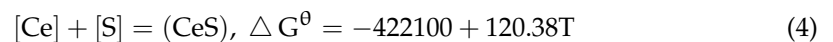
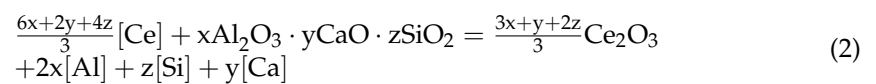
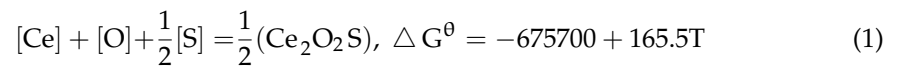


Figure 10. The evolution mechanism of main inclusions in the present study.

The subsequent inclusion evolution can be roughly divided into three paths according to the different Ce contents. When the content of Ce in molten steel is low (52 ppm), the $\text{Ce}_2\text{O}_2\text{S}$ inclusions are formed at steelmaking temperature. As the temperature decreases to the liquidus, MnS precipitates on the surface of the $\text{Ce}_2\text{O}_2\text{S}$ inclusions until the temperature drops to room temperature and the inclusions are composed of the $\text{Ce}_2\text{O}_2\text{S}$ -MnS composite. When the Ce content of molten steel increases to the moderate levels of 139 and 171 ppm, Ce reacts with S in molten steel to form CeS at the steelmaking temperature. Then, with the decrease in temperature, CeS will undergo phase transformation, from CeS to Ce_3S_4 and then to Ce_2S_3 . Some of these compounds embed on the surface of $\text{Ce}_2\text{O}_2\text{S}$. When the temperature further decreases to the liquidus temperature, MnS begins to precipitate on $\text{Ce}_2\text{O}_2\text{S}$. Finally, upon cooling to room temperature, the inclusion comprises $\text{Ce}_2\text{O}_2\text{S}$ -MnS- Ce_2S_3 . $\text{Ce}_2\text{O}_2\text{S}$ and CeS are also formed at high temperatures when the content of Ce in molten steel reaches 256 and 340 ppm, but no MnS was precipitated during the cooling process. The difference was that CeS completely transformed into Ce_2S_3 and Ce_3S_4 when Ce was 256 ppm, while CeS partially transforms into Ce_3S_4 when Ce was 340 ppm. The formation of sulfides in Ce can be described by Equations (4)–(6) [31].



3.5. Effect of Ce on Sulfide after Simulated Rolling

Figure 11 shows the distribution of the aspect ratio of inclusions after hot compression. The average aspect ratio of the inclusions in C0 was 2.77, while the aspect ratio of the inclusions after hot compression upon Ce addition was 1.54–1.83, which was significantly smaller than that of the former, indicating that the inclusions of Ce-added steel are still near-spherical after hot compression. Regarding the proportion of the inclusions with different aspect ratios, the proportions of the inclusions with varying aspect ratios in sample C0 were ~30%. Compared with those before rolling, as shown in Figure 8, the proportion of the inclusions with aspect ratios between one and two was significantly reduced, and the proportions of the inclusions with aspect ratios between two and three and larger than three were significantly increased, which indicates that MnS underwent deformation during hot compression. According to the change in the aspect ratios before and after simulated rolling, the change in the aspect ratio of the inclusion in C0 was 45.79%. In contrast, the aspect ratios of C1 to C5 upon Ce addition changed negligibly, indicating that MnS is not elongated. This confirms that Ce can well inhibit the deformation of MnS during rolling. Based on the calculation results for the number density and size of inclusions, the inclusions in C2 have a high number density and a small size. Therefore, to obtain numerous small and dispersed deformation-resistant inclusions in U75V heavy rail steel, the Ce content must be controlled at 139 ppm.

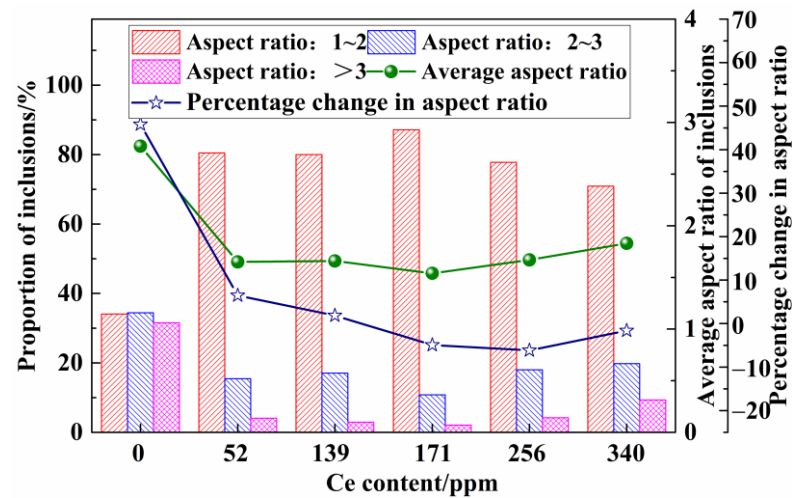


Figure 11. Aspect ratio of inclusions after simulated rolling.

4. Conclusions

This study analyzed the composition, two-dimensional and three-dimensional morphologies, number density, and size of the inclusions in heavy rail steel with different Ce contents. The evolution of the inclusions after Ce addition was discussed, and the effect of added Ce on modified MnS was investigated in terms of the aspect ratio of the inclusions before and after thermal deformation. The conclusions are as follows:

- (1) Without Ce addition to steel, the inclusions in heavy rail steel were elongated MnS and irregular Al-Si-Ca-O inclusions. With the increase in the Ce content from 52 to 340 ppm, the composition of the main inclusions changed in order of $\text{Ce}_2\text{O}_2\text{S-MnS} \rightarrow \text{Ce}_2\text{O}_2\text{S-MnS-Ce}_2\text{S}_3 \rightarrow \text{Ce}_2\text{O}_2\text{S-Ce}_3\text{S}_4\text{-Ce}_2\text{S}_3 \rightarrow \text{Ce}_2\text{O}_2\text{S-Ce}_3\text{S}_4\text{-CeS}$.
- (2) The addition of Ce to molten steel causes a significant increase in the number density and a considerable reduction in the size and aspect ratio of the inclusions. The average size of the inclusions without Ce was $6.74 \mu\text{m}$. The average size of inclusions upon Ce addition was $2.01\text{--}4.04 \mu\text{m}$, the size of inclusions was the smallest at 139 ppm Ce.
- (3) The change in the aspect ratio of the inclusions before and after thermal deformation was minimal, indicating that Ce can significantly inhibit the deformation of inclusions during the hot compression process. Therefore, when the Ce content of molten steel was 139 ppm, substantial amounts of dispersed, fine, and deformation-resistant inclusions can be obtained.

Author Contributions: Conceptualization, C.Z. and Y.S.; methodology, C.Z. and Y.S.; software, C.Z.; validation, C.Z., R.L. and Z.Z.; formal analysis, Y.Z.; investigation, R.L. and X.H.; resources, R.L.; data curation, C.Z.; writing—original draft preparation, C.Z.; writing—review and editing, C.Z. and H.W.; visualization, C.Z.; supervision, Y.S.; project administration, Y.S.; funding acquisition, Y.S. All authors have read and agreed to the published version of the manuscript.

Funding: This research was funded by the National Natural Science Foundation of China, grant number 51774030.

Institutional Review Board Statement: Not applicable.

Informed Consent Statement: Not applicable.

Data Availability Statement: Not applicable.

Acknowledgments: The authors gratefully acknowledge Zhaobo Wu in Central Iron and Steel Research Institute for his help and support with the ASPEX analysis.

Conflicts of Interest: The authors declare no conflict of interest. The funding sponsors had no role in the choice of the research project; the design of the study; the collection, analysis or interpretation of data; the writing of the manuscript; or the decision to publish the results.

References

1. Luu, W.; Wu, J. Effects of sulfide inclusion on hydrogen transport in steels. *Mater. Lett.* **1995**, *24*, 175–179. [[CrossRef](#)]
2. Garet, M.; Brass, A.M.; Haut, C.; Gutteriez-Solana, F. Hydrogen trapping on non metallic inclusions in Cr-Mo low alloy steels. *Corros. Sci.* **1998**, *40*, 1073–1086. [[CrossRef](#)]
3. Domizzi, G.; Anteri, G.; Ovejero-Garcia, J. Influence of sulphur content and inclusion distribution on the hydrogen induced blister cracking in pressure vessel and pipeline steels. *Corros. Sci.* **2001**, *43*, 325–339. [[CrossRef](#)]
4. Wu, X.; Wu, L.; Xie, J.; Shen, P.; Fu, J. Modification of sulfide by Te in Y₁Cr₁₃ free-cutting stainless steel. *Metall. Res. Technol.* **2020**, *117*, 107. [[CrossRef](#)]
5. Brimacombe, J.K.; Sorimachi, K. Crack formation in the continuous casting of steel. *Metall. Trans. B* **1977**, *8*, 489–505. [[CrossRef](#)]
6. Oikawa, K.; Ishida, K.; Nishizawa, T. Effect of titanium addition on the formation and distribution of MnS inclusions in steel during solidification. *ISIJ Int.* **1997**, *37*, 332–338. [[CrossRef](#)]
7. Xie, J.; Zhang, D.; Yang, Q.; An, J.; Huang, Z.; Fu, J. Exploration of morphology evolution of the inclusions in Mg-treated 16MnCrS5 steel. *Ironmak. Steelmak.* **2018**, *46*, 564–573. [[CrossRef](#)]
8. Lu, J.; Cheng, G.; Chen, L.; Xiong, G.; Wang, L. Distribution and morphology of MnS inclusions in resulfurized non-quenched and tempered steel with Zr addition. *ISIJ Int.* **2018**, *58*, 1307–1315. [[CrossRef](#)]
9. Blais, C.; L'Espérance, G.; LeHuy, H.; Forget, C. Development of an integrated method for fully characterizing multiphase inclusions and its application to calcium-treated steels. *Mater. Charact.* **1997**, *38*, 25–37. [[CrossRef](#)]
10. Chen, L. Study on the effects of Ti micro-addition on the characteristics of MnS inclusions in rail steel. *Ironmak. Steelmak.* **2019**, *46*, 508–512. [[CrossRef](#)]
11. Ji, S.; Zhang, L.; Wang, X. Effect of Magnesium on Inclusions in a High Sulfur Steel. *Metall. Mater. Trans. B* **2022**, *53*, 848–863. [[CrossRef](#)]
12. Shen, P.; Fu, J. Morphology study on inclusion modifications using Mg–Ca treatment in resulfurized special steel. *Materials* **2019**, *12*, 197. [[CrossRef](#)] [[PubMed](#)]
13. Guo, Y.; He, S.; Chen, G.; Wang, Q. Thermodynamics of complex sulfide inclusion formation in Ca-treated Al-killed structural steel. *Metall. Mater. Trans. B* **2016**, *47*, 2549–2557. [[CrossRef](#)]
14. Wang, H.; Xiong, L.; Zhang, L.; Wang, Y.; Shu, Y.; Zhou, Y. Investigation of RE-OS-As inclusions in high carbon steels. *Metall. Mater. Trans. B* **2017**, *48*, 2849–2858. [[CrossRef](#)]
15. Adabavazeh, Z.; Hwang, W.; Su, Y. Effect of adding cerium on microstructure and morphology of Ce-based inclusions formed in low-carbon steel. *Sci. Rep.* **2017**, *7*, 46503. [[CrossRef](#)] [[PubMed](#)]
16. Wang, H.; Bao, Y.; Zhao, M.; Wang, M.; Yuan, X.; Gao, S. Effect of Ce on the cleanliness, microstructure and mechanical properties of high strength low alloy steel Q690E in industrial production process. *Int. J. Miner. Metall. Mater.* **2019**, *26*, 1372–1384. [[CrossRef](#)]
17. Wang, X.; Li, G.; Liu, Y.; Wang, F.; Wang, Q. Cerium Addition Effect on Modification of Inclusions, Primary Carbides and Microstructure Refinement of H13 Die Steel. *ISIJ Int.* **2021**, *61*, 1850–1859. [[CrossRef](#)]
18. Torkamani, H.; Raygan, S.; Mateo, C.G.; Rassizadehghani, J.; Vivas, J.; Palizdar, Y.; San-Martin, D. The influence of La and Ce addition on inclusion modification in cast niobium microalloyed steels. *Metals* **2017**, *7*, 377. [[CrossRef](#)]
19. Ren, Q.; Zhang, L. Effect of cerium content on inclusions in an ultra-low-carbon aluminum-killed steel. *Metall. Mater. Trans. B* **2020**, *51*, 589–600. [[CrossRef](#)]
20. Liu, Z.; Song, B.; Yang, Z.; Cui, X.; Li, L.; Wang, L.; Song, Z. Effect of Cerium Content on the Evolution of Inclusions and Formation of Acicular Ferrite in Ti-Mg-Killed EH36 Steel. *Metals* **2020**, *10*, 863. [[CrossRef](#)]
21. Liu, H.; Fu, P.; Liu, H.; Sun, C.; Sun, M.; Li, D. A novel large cross-section quenching and tempering mold steel matching excellent strength–hardness–toughness properties. *Mat. Sci. Eng. A* **2018**, *737*, 274–285. [[CrossRef](#)]
22. Liu, Y.; Wang, L.; Chou, K. Effect of cerium on the cleanliness of spring steel used in fastener of high-speed railway. *J. Rare Earths* **2014**, *32*, 759–766. [[CrossRef](#)]
23. Gao, S.; Wang, M.; Guo, J.; Wang, H.; Zhi, J.; Bao, Y. Characterization Transformation of Inclusions Using Rare Earth Ce Treatment on Al-Killed Titanium Alloyed Interstitial Free Steel. *Steel Res. Int.* **2019**, *90*, 1900194. [[CrossRef](#)]
24. Luo, S.; Shen, Z.; Yu, Z.; Wang, W.; Zhu, M. Effect of Ce Addition on Inclusions and Grain Structure in Gear Steel 20CrNiMo. *Steel Res. Int.* **2021**, *92*, 2000394. [[CrossRef](#)]
25. Wang, Y.; Li, C.; Wang, L.; Xiong, X.; Chen, L.; Zhuang, C. Modification of Alumina Inclusions in SWRS82B Steel by Adding Rare Earth Cerium. *Metals* **2020**, *10*, 1696. [[CrossRef](#)]
26. Zhang, J.; Yu, Y.; Wang, S.; Hou, Y.; Yin, S. Effects of Rare Earth on Mechanical Properties of LZ50 Axle Steels and Its Formation Mechanism. *High Temp. Mater. Process* **2018**, *37*, 509–519. [[CrossRef](#)]
27. Cai, G.; Pang, Y.; Huang, Y.; Misra, R.D.K. Roles of Inclusion, Texture and Grain Boundary in Corrosion Resistance of Low-Nickel Austenite Stainless Steel Containing Ce. *ISIJ Int.* **2019**, *59*, 2302–2310. [[CrossRef](#)]
28. Shen, P.; Yang, Q.; Zhang, D.; Yang, S.; Fu, J. The effect of tellurium on the formation of MnTe-MnS composite inclusions in non-quenched and tempered steel. *Metals* **2018**, *8*, 639. [[CrossRef](#)]
29. Li, X.; Jiang, Z.; Geng, X.; Chen, M.; Peng, L. Evolution mechanism of inclusions in H13 steel with rare earth magnesium alloy addition. *ISIJ Int.* **2019**, *59*, 1552–1561. [[CrossRef](#)]

-
30. Gong, W.; Wang, P.; Zhang, L.; Jiang, Z. Effects of Ce on Microstructure and Mechanical Properties of LDX2101 Duplex Stainless Steel. *Metals* **2020**, *10*, 1233. [[CrossRef](#)]
 31. Li, X.; Jiang, Z.; Geng, X.; Chen, M.; Cui, S. Effect of Rare Earth–Magnesium Alloy on Inclusion Evolution in Industrial Production of Die Steel. *Steel Res. Int.* **2019**, *90*, 1900103. [[CrossRef](#)]